
White Rose Research Online

eprints@whiterose.ac.uk
https://eprints.whiterose.ac.uk
Universities of Leeds, Sheffield and York

Deposited via The University of Sheffield.

White Rose Research Online URL for this paper:
https://eprints.whiterose.ac.uk/id/eprint/247200/

Version: Published Version

Article:
Singh, A., Ranot, H., Kumar, M. et al. (2026) Pressureless liquid-phase sintering of copper with a mechanically milled Cu–Ag eutectic-composition premix. Powder Metallurgy. ISSN: 0032-5899

https://doi.org/10.1177/00325899261493581

Reuse
This article is distributed under the terms of the Creative Commons Attribution-NonCommercial (CC BY-NC) licence. This licence allows you to remix, tweak, and build upon this work non-commercially, and any new works must also acknowledge the authors and be non-commercial. You don't have to license any derivative works on the same terms. More information and the full terms of the licence here:
https://creativecommons.org/licenses/

Takedown
If you consider content in White Rose Research Online to be in breach of UK law, please notify us by emailing eprints@whiterose.ac.uk including the URL of the record and the reason for the withdrawal request.

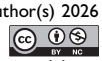




Check for updates

Original research article

I·M3 Institute of Materials, Minerals & Mining

Powder Metallurgy
1–15
© The Author(s) 2026

Article reuse guidelines:
sagepub.com/journals-permissions
DOI: 10.1177/00325899261493581
journals.sagepub.com/home/pmg

Sage

Pressureless liquid-phase sintering of copper with a mechanically milled Cu–Ag eutectic-composition premix

Avinash Singh[1], Harish Ranot[2], Mirtunjay Kumar[3] and Anish Upadhyaya[1]

Abstract

Pressureless liquid-phase sintering of Cu containing a mechanically milled 28Cu–72Ag (wt.%) premix was investigated to relate premix content and thermal history to densification, microstructure, hardness and electrical conductivity. Cu blends containing 0–40 wt.% premix were processed using five schedules that varied heating rate and holding time. Increasing premix content enhanced densification despite lowering green density. D120–Cu–40Et gave the largest mean relative density (~93.4%), while H20–Cu–40Et reached ~92.2% after 15 minutes at 800 °C. Longer high-temperature exposure refined pores and increasingly rounded Cu-rich regions at higher premix contents, whereas rapid heating retained finer, heterogeneous Ag-rich intergranular regions. X-ray diffraction and energy-dispersive spectroscopy identified mutually soluble Cu-rich and Ag-rich face-centred-cubic phases without additional crystalline intermetallics. When combined hardness and conductivity are prioritised, with density and hold duration as trade-offs, H20–Cu–40Et is the single recommended tested condition: (67.9 ± 2.3) $HV_{0.1}$ and (77.9 ± 2.0)% IACS. D120–Cu–40Et is the density benchmark, not a second overall optimum; the recommendation is based on observed means without significance testing.

Keywords

Cu–Ag alloy, powder metallurgy, liquid-phase sintering, electrical conductivity, microstructural evolution

Received: 27 June 2026; accepted: 12 September 2026

Introduction

Copper combines high electrical and thermal conductivity with good manufacturability, but its modest strength and hardness limit components exposed to mechanical loading, wear or dimensional change.[1–3] Alloying, deformation and microstructural refinement can strengthen Cu, yet the resulting solutes, dislocations, grain boundaries and phase interfaces also scatter electrons.[3,4] High-strength Cu conductors must therefore balance mechanical performance and electron transport through composition and microstructural design.[3,5,6]

The Cu–Ag system is attractive because both elements conduct well and their limited mutual solid solubility permits Cu-rich and Ag-rich constituents.[7] Ag-rich precipitates, eutectic colonies and nanotwins can strengthen the alloy while retaining metallic conduction paths.[8–10] Filamentary Cu–Ag microcomposites can likewise combine high strength with useful conductivity.[11–13] Precipitate size, strain and distribution depend on ageing and microalloying.[14–16] Deformation further changes microstructure, resistivity and tensile response.[17–19] Strong, conductive cast, rolled and wire-drawn Cu–Ag products have been reported, but their controlled solidification, extensive deformation and intermediate heat treatments are less suited to near-net-shape parts.[11,20,21]

Powder processing controls the proportions and initial distribution of Cu and Ag. Spark-plasma sintering, hot pressing and electroless Ag deposition have produced Cu–Ag conductors.[22,23] Laser powder-bed fusion has also been applied to Cu–Ag alloys.[24] In gas-atomised Cu–Ag powder, ageing can produce conductive Ag networks along grain boundaries within the particles and improve oxidation resistance.[25] Pressureless sintering is simpler than pressure-assisted consolidation but is more sensitive to surface condition, gas removal, packing and solid-state transport.[26–28] A liquid-forming addition may improve densification without external pressure.

Liquid-phase sintering promotes particle rearrangement, solution-mediated transport and pore removal; its effectiveness depends on liquid fraction, wetting, solubility, packing and thermal exposure.[27,29–32] The liquid may persist during

[1]Department of Materials Science and Engineering, Indian Institute of Technology Kanpur, Kanpur, UP, India
[2]School of Minerals, Metallurgical and Materials Engineering, Indian Institute of Technology Bhubaneswar, Bhubaneswar, OD, India
[3]Department of Materials Science and Engineering, The University of Sheffield, Sheffield, South Yorkshire, UK

Corresponding authors:
Mirtunjay Kumar, Department of Materials Science and Engineering, The University of Sheffield, Sheffield S1 3JD, South Yorkshire, UK.
Email: m.kumar@sheffield.ac.uk

Anish Upadhyaya, Department of Materials Science and Engineering, Indian Institute of Technology Kanpur, Kanpur, UP 208016, India.
Email: anishu@iitk.ac.in

holding or be consumed by diffusion or reaction.[27,31,32] Near the Cu–Ag eutectic, liquid forms below the melting points of pure Cu and Ag while Ag dissolves in Cu-rich solid.[7] Its fraction and composition therefore evolve during heating and holding, and any remaining liquid solidifies on cooling. Mechanical milling can disperse Cu and Ag but also changes particle shape, strain and agglomeration, thereby affecting compactibility.[33,34] High-strain processing can also refine lamellae, promote mechanical alloying and produce nonequilibrium Cu/Ag distributions.[35–37]

Few studies have combined pressureless sintering with a mechanically milled liquid-forming Cu–Ag premix or varied premix content, sub-eutectic holding, high-temperature holding and heating rate within one series. Here, Cu was blended with 0–40 wt.% of a 28Cu–72Ag (wt.%) premix and sintered using five schedules. The practical objective is to identify a pressureless-sintered Cu–Ag condition combining high electrical conductivity with high hardness. We therefore prioritise these two measured properties together and evaluate the associated density and hold-duration trade-offs, rather than selecting solely for maximum density. This qualitative criterion is used to recommend one condition within the tested range.

Experimental procedure

Starting powders and material compositions

Elemental Cu and Ag powders of 99.9% purity were used. The gas-atomised Cu powder was supplied by GKN Powder Metallurgy, and the Ag powder by Innomet Powders. SEM-based mean particle sizes were ~9.8 μm for Cu and 5.2 μm for Ag. For the matrix Cu powder, the apparent density, tap density and Hall flow time were 36.4% of theoretical density, 43.5% of theoretical density and 27 seconds per 50 g, respectively.[38–40]

Powder morphology was examined by secondary-electron SEM (JEOL JSM-7100F) after dispersion in methanol, ultrasonication for 1 hour and drying. Particle sizes were measured manually in ImageJ.[41] A mechanically milled 28Cu–72Ag (wt.%) premix, denoted Et, was added to Cu at 0, 10, 20, 30 and 40 wt.%. Table 1 gives Ag contents calculated from the weighed masses; the milled Et was not chemically analysed. Cu–40Et was the highest addition studied. The starting powders and milled premix are shown in Figure 1.

In the figures, w_{Et} denotes the Et-premix content of the powder blend in wt.%, and w_{Ag} denotes the local Ag content measured by EDS in wt.%.

The nominal theoretical density was calculated from the inverse rule of mixtures,

$$\rho_{th,nom} = \left(\sum_{i=1}^{n} \frac{w_i}{\rho_i} \right)^{-1} \quad (1)$$

where w_i and ρ_i are the mass fraction and theoretical density of component i, respectively. The calculations used $\rho_{Cu} = 8.92\ g\,cm^{-3}$ and $\rho_{Ag} = 10.49\ g\,cm^{-3}$. The resulting $\rho_{th,nom}$ assumes ideal volume additivity.

Preparation of the Cu–Ag eutectic-composition premix

Cu and Ag powders were weighed to mass fractions of 0.28 and 0.72, respectively. They were mixed for 1 hour in a Turbula mixer and wet milled for a total of 24 hours in a Fritsch P-5 planetary mill. WC balls, a 10:1 ball-to-powder mass ratio and acetone were used in an Ar-sealed vial. The powder was dried at 70 °C and blended with Cu for 2 hours. Masses were measured to 0.001 g. Figure 2 summarises the premix preparation and subsequent blending route.

Table 1. Powder-blend compositions and nominal theoretical densities. Et denotes the mechanically milled 28Cu–72Ag (wt.%) premix.

Material	Et addition (wt.%)	Total Ag (wt.%)	$\rho_{th,nom}$ (g cm^{-3})
Cu	0	0.00	8.920
Cu–10Et	10	7.20	9.017
Cu–20Et	20	14.40	9.116
Cu–30Et	30	21.60	9.218
Cu–40Et	40	28.80	9.322

Compaction

The blended powders were compacted by single-action uniaxial pressing in a cylindrical steel die at 250 MPa for 30 seconds. Zinc stearate was applied to the die wall and punch surfaces after cleaning with acetone. The green compacts were ~16 mm in diameter and 6 mm in height. Three independently pressed and sintered compacts were prepared for each composition–schedule condition.

Preheating and sintering schedules

Specimens on an alumina support were sintered in a programmable horizontal tube furnace (OKAY 70T-4, Bysakh and Co., India). After a 15 minute Ar purge, dry H_2 (dew point approximately −35 °C) flowed at 0.5 L min^{-1} during heating, holding and furnace cooling. Hydrogen reduces Cu surface oxides that can inhibit neck formation and consolidation.[42,43] All specimens were preheated at 250 °C for 1 h; Table 2 gives the subsequent schedules.

The Cu–Ag eutectic temperature is ~779.1 °C at 71.6 wt.% Ag[7]; thus, the 72 wt.% Ag premix was heated about 21 °C above this temperature. No DSC or DTA was performed. Because milling can alter strain and Cu/Ag distribution, the equilibrium diagram guided temperature selection but does not establish the premix melting interval.[33,34,37]

At 800 °C, the phase diagram gives ~7.5 wt.% Ag in the Cu-rich solid and 67 wt.% in the liquid.[7] Cu–10Et (7.20 wt.% Ag) lies just below the solidus, although Et-rich contacts may melt temporarily. Cu–20Et, Cu–30Et and Cu–40Et lie in the solid + liquid field, with lever-rule liquid fractions of ~12, 24 and 36 wt.%. These are equilibrium estimates, not measured liquid fractions.[7,27]

Density and dimensional measurements

Green density was calculated geometrically from the compact mass, diameter and height:

$$\rho_g = \frac{4m_g}{\pi D_g^2 L_g} \quad (2)$$

where m_g, D_g and L_g are the green mass, diameter and height, respectively. Sintered density was measured by the

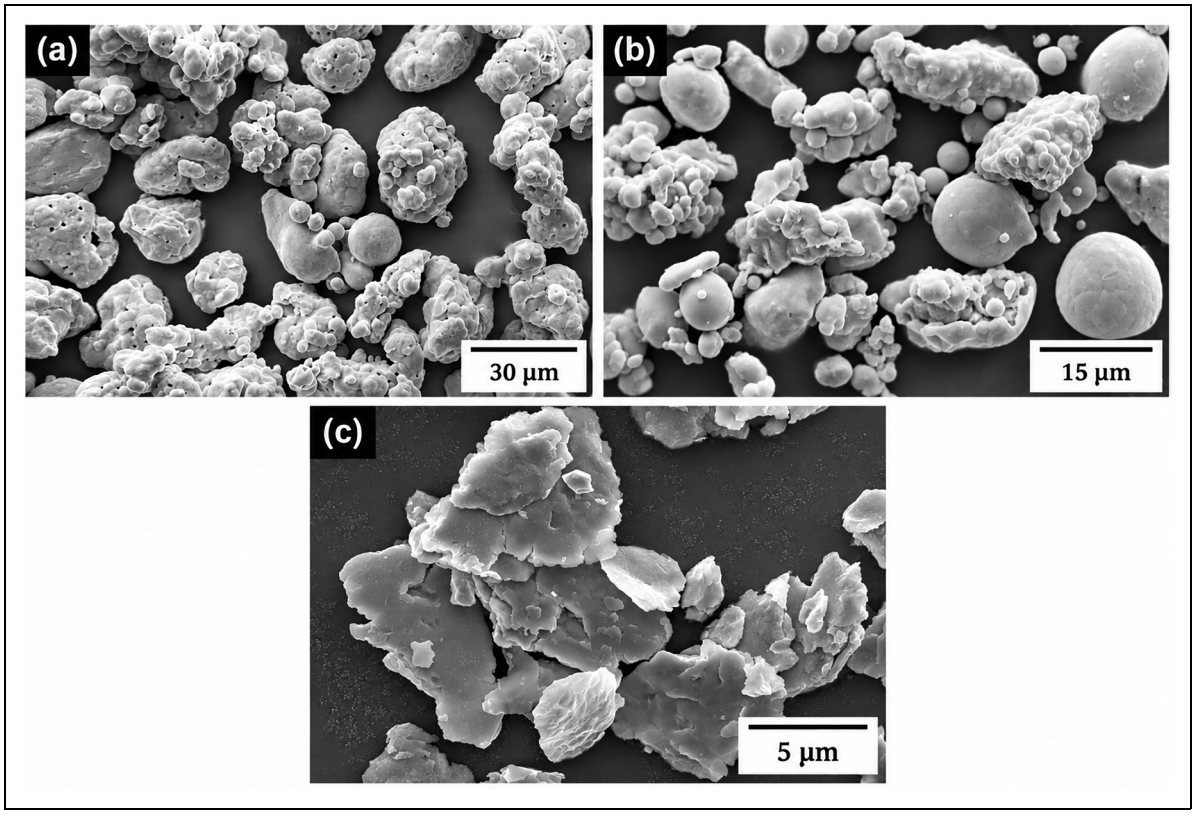


Figure 1. Starting powders: (a) Cu powder, (b) Ag powder and (c) mechanically milled 28Cu–72Ag (wt.%) premix.

Archimedes method in distilled water.[44] Specimens with open porosity were vacuum-impregnated before immersion to limit water penetration. For an impregnated specimen, the dry bulk density is expressed as follows:

$$\rho_s = \frac{m_{dry}\rho_w}{m_{imp,air} - m_{imp,water}} \tag{3}$$

where m_{dry} is the dry sintered-specimen mass before impregnation, $m_{imp,air}$ is the impregnated-specimen mass in air after removal of excess surface impregnant, $m_{imp,water}$ is its apparent immersed mass corrected for the suspension support, and ρ_w is the water density at the measurement temperature. This expression assumes that accessible pores are saturated and that the impregnant adds negligible external volume; an appreciable external coating requires a volume correction. Relative densities were calculated using the nominal theoretical densities in Table 1, and the densification parameter was defined as follows:

$$\Phi = \frac{\rho_s - \rho_g}{\rho_{th,nom} - \rho_g} \tag{4}$$

where ρ_g, ρ_s and $\rho_{th,nom}$ are the green, sintered and nominal theoretical densities, respectively, and Φ is the densification parameter. Axial and radial dimensions were measured before and after sintering using a Vernier calliper, and shrinkage was calculated as follows:

$$S_a = \left(1 - \frac{L_s}{L_g}\right) \times 100 \tag{5}$$

and

$$S_r = \left(1 - \frac{D_s}{D_g}\right) \times 100 \tag{6}$$

where L_s and D_s are the sintered height and dia, respectively. Positive values denote shrinkage, and S_a/S_r was used to compare shrinkage anisotropy.

For cylindrical specimens, density and dimensional changes are related by the specimen-level mass–volume balance

$$\frac{R_s}{R_g} = \frac{m_{dry}}{m_g} \frac{1}{(1 - S_a/100)(1 - S_r/100)^2} \tag{7}$$

where $R_g = \rho_g/\rho_{th,nom}$ and $R_s = \rho_s/\rho_{th,nom}$ are relative densities expressed as fractions, and m_{dry} is the dry sintered mass defined in equation (3). This relation assumes that the measured diameters and heights represent the specimen volumes and that the same nominal theoretical density is used before and after sintering. The green mass and dimensions must refer to the same specimen state. A consistency check requires paired specimen measurements; substituting condition means does not generally preserve this nonlinear relation.

Metallographic preparation and microstructural analysis

Sintered specimens were sectioned, mounted in epoxy, ground with 220–1200 grit SiC paper and polished with 1 μm and 0.3 μm alumina. Selected specimens were etched with an $FeCl_3$-based reagent.[45] Secondary- and backscattered-electron SEM images showed porosity and the Cu-rich and Ag-rich regions. Quantitative measurements were made in ImageJ on micrographs containing sufficient regions, pores and interfaces.

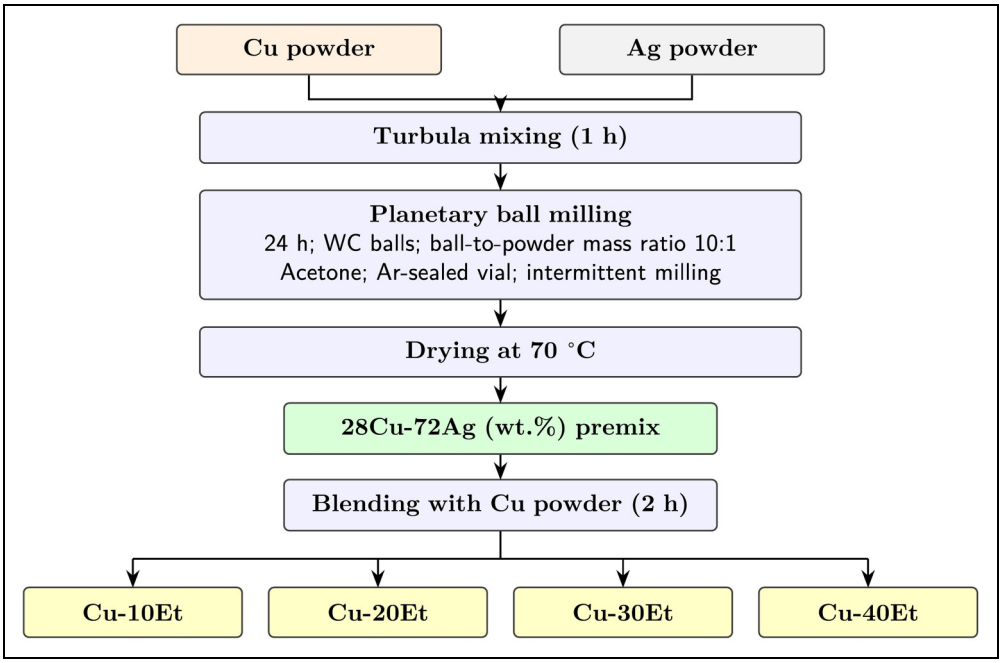


Figure 2. Preparation of the mechanically milled 28Cu–72Ag (wt.%) premix and the Cu–Et powder blends. Et denotes the premix; Cu–10Et to Cu–40Et contain 10–40 wt.% premix, respectively. The unalloyed Cu control does not undergo this premix-preparation route.

Quantitative stereology

The size of the visible Cu-rich regions was described by calibrated lineal intercepts across unetched BSE micrographs covering ~3 mm^2.[46,47] Each intercept ended where grey Cu-rich contrast met a bright Ag-rich region or dark pore; contrast variations within a connected grey region were ignored. Because these boundaries were not validated by EBSD, the intercepts are not interpreted as measurements of crystallographic or ASTM grain size.

At least 500 complete intercepts were measured per condition. Image-edge intercepts were excluded, which may under-represent larger regions. The reported analysis protocol summarises the pooled intercepts by a Weibull-fit median, denoted ℓ_{Cu}, without specimen-level uncertainty. However, the retained schematic in Figure 3 refers to a mean linear intercept and ASTM E112, while Figure 4(a) labels the plotted quantity as 'Grain size, d_g'. These descriptions are not interchangeable. The correspondence between the plotted values and the reported median-intercept protocol remains to be verified from the measurement exports and fit records. Accordingly, panel (a) is discussed below only as a plotted Cu-rich size descriptor, not as a verified median intercept or crystallographic grain size, and is not used for statistical schedule ranking.

Pores were segmented with the Trainable Weka Segmentation plugin.[41,48] The method description identifies d_p as a Feret diameter, whereas the retained schematic specifies an equivalent-circle diameter. The latter is $d_{eq} = 2\sqrt{A/\pi}$ for pore cross-sectional area A and is not generally equal to a Feret diameter. The exported diameter definition and plotted summary statistic remain unverified; a Feret-based analysis additionally requires identification of the maximum, minimum or directional diameter used. Therefore, d_p is retained only as the pore-size descriptor labelled in Figure 4(b), without assigning either diameter definition to those values.

Contiguity of the Cu-rich regions was calculated as follows:

$$C_s = \frac{2N_{ss}}{2N_{ss} + N_{sl}} \tag{8}$$

where N_{ss} and N_{sl} are the Cu-rich–Cu-rich and Cu-rich–Ag-rich contacts intersected by the test lines. Both refer to post-cooling phase contacts. The subscripts and solid–liquid terminology retained in Figure 3 are schematic conventions, not evidence of liquid present during imaging. Approximately 200 identifiable dihedral angles, ϕ, were measured per condition with the ImageJ angle tool.[49,50] These are apparent two-dimensional post-cooling junction angles, not direct equilibrium melt-wetting angles.

Table 2. Thermal schedules used for sintering the Cu–Et materials. All schedules were preceded by preheating at 250 °C for 1 hour.

Code	Thermal schedule
D15	Heating at 5 °C min^{-1} to 800 °C, followed by a 15 minutes isothermal hold
D120	Heating at 5 °C min^{-1} to 800 °C, followed by a 120 minutes isothermal hold
I60	Heating at 5 °C min^{-1} to 600 °C, holding for 60 minutes, followed by heating to 800 °C and holding for 15 minutes
I120	Heating at 5 °C min^{-1} to 600 °C, holding for 120 minutes, followed by heating to 800 °C and holding for 15 minutes
H20	Heating at 20 °C min^{-1} to 800 °C, followed by a 15 minutes isothermal hold

X-ray diffraction

Phase analysis used a PANalytical X'Pert diffractometer with Cu Kα radiation ($\lambda = 1.5406$ Å) at a scan rate of 2° min^{-1}. Peaks were indexed with the ICDD PDF-2 database and HighScore Plus. Patterns were compared across

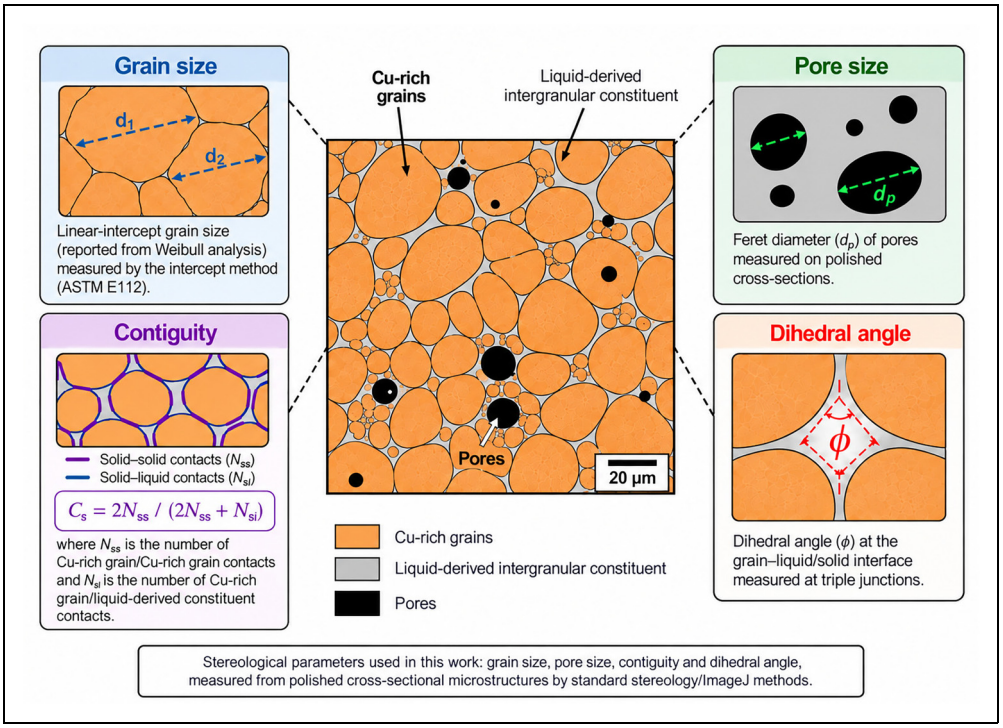


Figure 3. Schematic of size, contiguity and junction-angle measurements, shown in named boxes. The retained 'Grain size' box illustrates a mean-intercept construction and cites ASTM E112; it does not establish crystallographic grain size or the Weibull-fit median ℓ_{Cu} described in the methods. The pore-size box illustrates an equivalent-circle diameter, which differs from the Feret diameter named in the method description. Neither discrepancy is resolved by this schematic; the plotted size definitions require verification. For the post-cooling observations, solid–solid and solid–liquid labels are interpreted as Cu-rich–Cu-rich and Cu-rich–Ag-rich contacts, respectively, and ϕ as an apparent two-dimensional junction angle, not an equilibrium melt-wetting angle.

compositions; the principal Cu-rich reflection provided the lattice parameter, crystallite size and microstrain, the latter two by pseudo-Voigt variance analysis.[51–53]

Energy-dispersive X-ray spectroscopy

Cu and Ag distributions were examined by EDS with an Oxford X-MAX v1 detector.[54] Maps compared Cu-rich and Ag-rich regions among schedules. Post-cooling spot analyses represent local final solids, not area averages or the liquid composition at 800 °C. Line scans across selected interfaces measured Cu K and Ag L signal changes; intermediate values and profile widths were interpreted with regard to the SEM–EDS interaction volume.

Hardness and conductivity measurements

Vickers hardness was measured on polished specimens using a Tinius-Olsen FH-10 hardness tester with a 100 gf load and 10 seconds dwell time.[55] Values are reported as $HV_{0.1}$. Electrical conductivity was measured on flat polished surfaces using a Technofour CM-979 eddy-current conductivity meter calibrated with annealed Cu of 99.5% IACS. ASTM E1004-17 is cited for the eddy-current measurement principle, rather than to claim full procedural compliance.[56] Results are reported as % IACS.

Statistical reporting

The compact was the experimental unit for density, dimensional change, hardness and conductivity ($n = 3$ independently processed compacts per condition). Figures 5 and 6 report condition means; specimen-level dispersion was not available for every condition and is therefore not reconstructed retrospectively. In Figure 7(a) and (b), error bars denote one standard deviation for the three compacts. The stereological values were pooled from fields on selected sections and are descriptive sampling measures rather than independent specimen replicates. No null-hypothesis significance tests were applied. Accordingly, comparative terms refer to observed means or descriptive values and do not imply statistically significant differences.

Results

Starting powders and processing design

Figure 1 shows the starting Cu and Ag powders (a,b) and the milled premix (c), while Figure 2 summarises the premix-preparation and blending route. The Cu and Ag powders were mainly rounded, with some irregular particles and satellites, and had mean sizes of ~9.8 and 5.2 μm, respectively. Milling converted the premix into irregular, flattened agglomerates through deformation, fracture and cold welding.[33,34] This morphology can impair packing but supplies the liquid-forming constituent during sintering.

Here, 'eutectic-composition premix' refers to the weighed 28Cu–72Ag (wt.%) mixture, close to the equilibrium eutectic at 71.6 wt.% Ag[7]; the term does not establish local compositional uniformity or the melting interval of the milled powder.

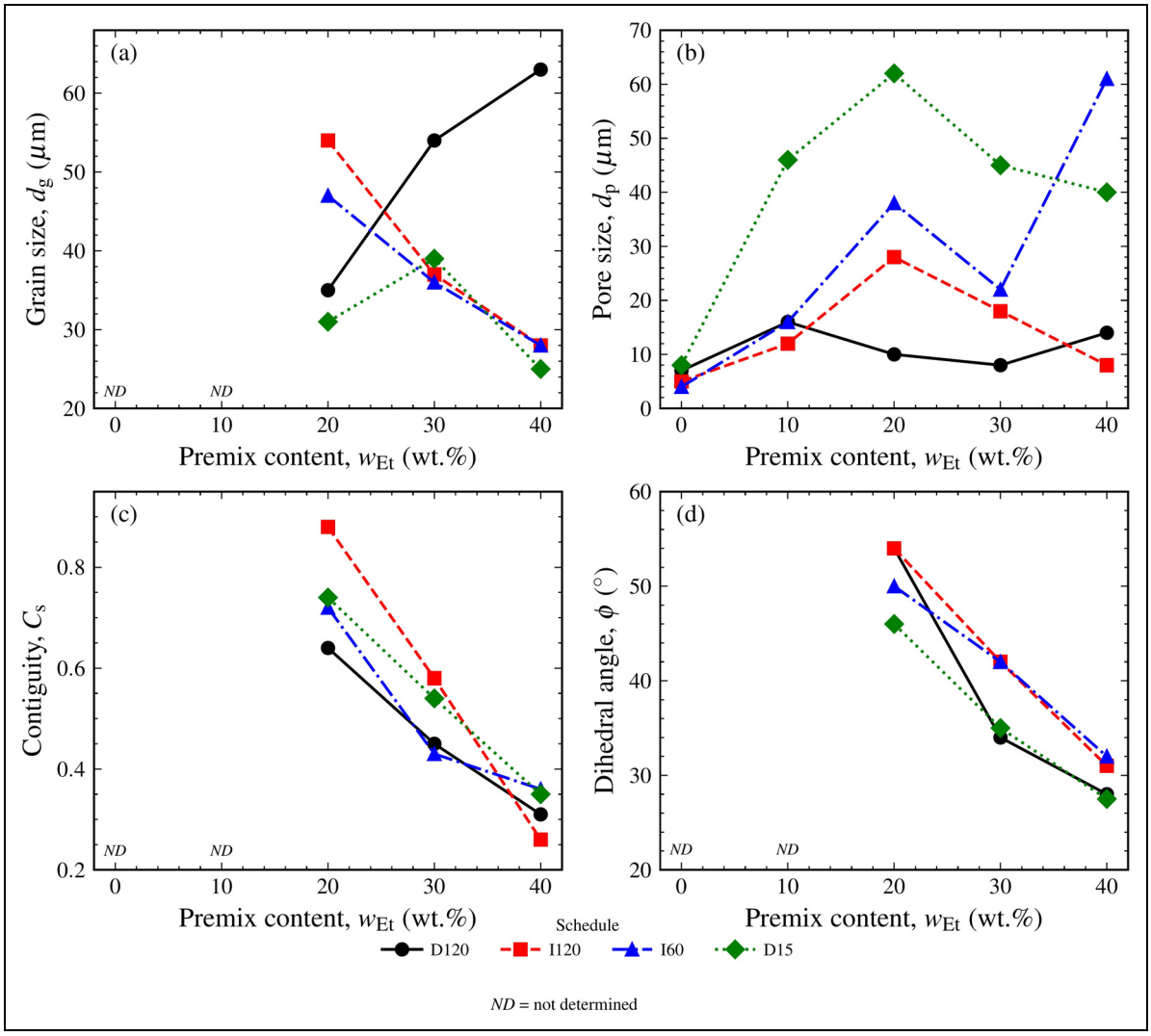


Figure 4. Descriptive stereology for D15, D120, I60 and I120: (a) Cu-rich size descriptor, retained under the artwork label 'Grain size, d_g'; (b) pore-size descriptor, d_p; (c) post-cooling Cu-rich-region contiguity, C_s; and (d) apparent two-dimensional post-cooling junction angle, ϕ. Panel (a) is not a validated crystallographic or ASTM grain-size measurement, and its correspondence to the reported Weibull-fit median intercept remains unverified. The diameter definition and summary statistic underlying panel (b) also remain unresolved; neither a Feret nor an equivalent-circle diameter is assigned here. The reported intercept protocol uses at least 500 complete intercepts per condition and excludes image-edge intercepts. Measurements were pooled from selected fields rather than treated as independent specimen replicates; no error bars or significance tests are assigned. ND denotes not determined.

Figure 8 shows the processing route and schedules. Preheating at 250 °C made the compact surfaces more uniform, consistent with removal of moisture, volatiles or gaseous products before pore closure.[26,27] All compacts retained their cylindrical shape after sintering.

Densification and dimensional response

Green density varied non-monotonically with premix content (Figure 5). Cu–10Et and Cu–20Et were comparable to or slightly denser than Cu, whereas Cu–30Et and Cu–40Et were less dense. At high additions, the irregular agglomerated premix impaired packing enough to outweigh the higher theoretical density of Ag.

Sintered density showed the opposite trend: except for Cu–10Et, relative density and densification increased towards Cu–30Et and Cu–40Et. Thus, the packing penalty was offset by greater liquid-forming content during sintering.[26,27] Cu–10Et responded less because its 7.20 wt.% Ag lies just below the Cu-rich solidus at 800 °C; any local liquid can disappear as Cu and Ag redistribute.[7]

The largest schedule-dependent differences in the observed means occurred at high premix contents. D120–Cu–40Et gave the largest mean relative density, ~93.4%, after 120 minutes at 800 °C. H20–Cu–40Et reached ~92.2% after only 15 minutes, consistent with rapid heating retaining sufficient liquid-forming capacity. Extending the intermediate hold from I60 to I120 also increased the mean Cu–40Et densification parameter.

The plotted axial and radial shrinkages generally increased with premix content (Figure 6), but their quantitative consistency with the reported densities remains unresolved. Axial shrinkage was usually greater; pressing-induced density gradients are a possible contributor.[57] Particle-orientation effects on shrinkage anisotropy have also been demonstrated in pressed alumina,[58] but their contribution in the present Cu–Ag compacts was not measured. The shrinkage ratio was therefore considered with

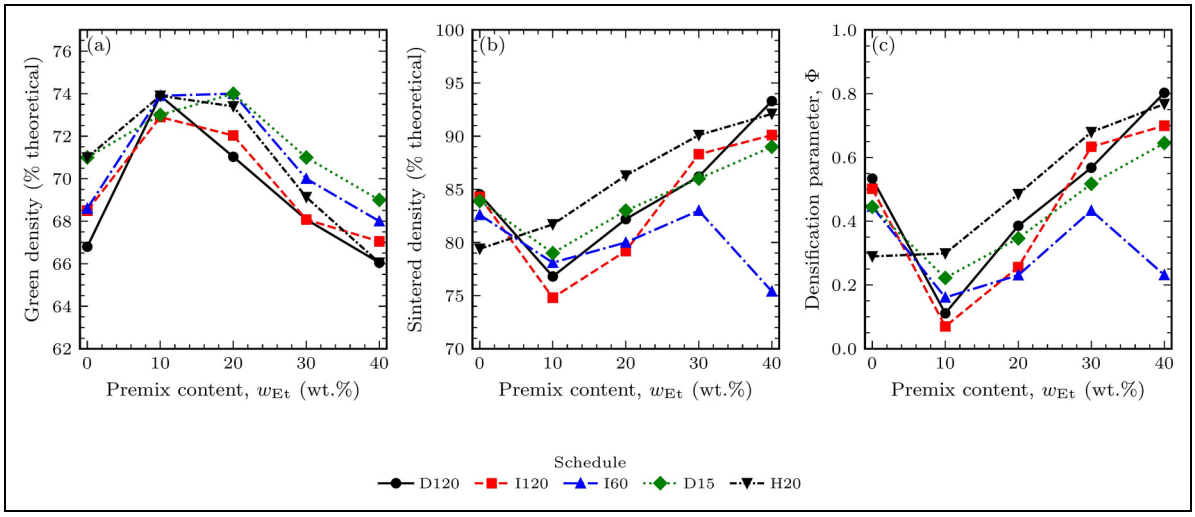


Figure 5. Effect of premix content and thermal schedule on (a) green relative density, (b) sintered relative density and (c) densification parameter. Points are condition means from three independently processed compacts; specimen-level dispersion was not available for every condition and no statistical significance is implied. Et denotes the mechanically milled 28Cu–72Ag (wt.%) premix.

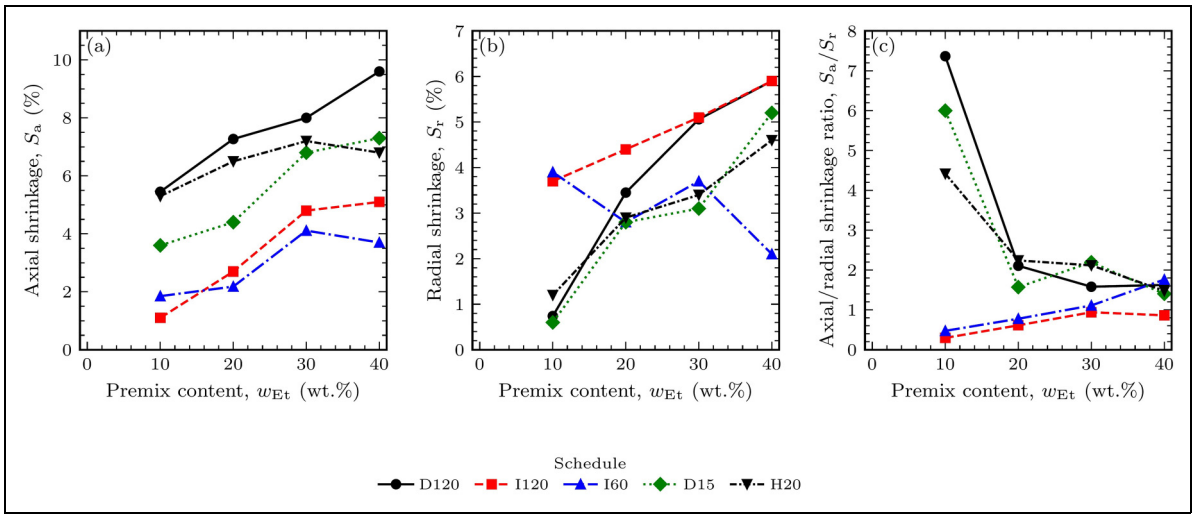


Figure 6. Dimensional response of the Cu–Et materials: (a) axial shrinkage, (b) radial shrinkage and (c) axial-to-radial shrinkage ratio. Points are condition means from three independently processed compacts; specimen-level dispersion was not available for every condition and no statistical significance is implied.

the absolute values rather than as an independent densification measure.

An approximate check using the plotted D120–Cu–40Et values, $R_g \approx 0.66$, $S_a \approx 9.6\%$ and $S_r \approx 5.9\%$, gives a sintered-to-green volume ratio of ~0.8005. Under dry-mass conservation, equation (7) then predicts $R_s \approx 0.825$, compared with the reported 0.934. Combining these plotted values instead implies a dry-mass ratio of ~1.133. A corresponding graph-based check for H20–Cu–40Et gives ~0.781 rather than 0.922, implying a dry-mass increase of about 18%. These implied increases are not measured mass gains. Although graph-reading uncertainty and averaging prevent a definitive specimen-level diagnosis, the discrepancies require reconciliation of paired dry masses, dimensions, density calculations and condition identifiers, including the timing of green measurements relative to preheating and any departure from cylindrical geometry. Until this reconciliation is complete, the reported density magnitudes, densification parameters and density-based trade-offs remain provisional; shrinkage cannot be treated as independent quantitative confirmation of densification.

Microstructure and stereological evolution

Increasing premix content changed the microstructure from a Cu-rich particle network with isolated pores to Cu-rich regions separated by bright Ag-rich material (Figures 9 and 10). Cu–10Et resembled unalloyed Cu, whereas Cu–20Et to Cu–40Et showed progressively clearer Ag-rich boundaries and junctions.

Extending the sub-eutectic hold from I60 to I120 refined the Cu–40Et pores and made the intergranular material more uniform. Under direct heating, D120 produced more rounded Cu-rich regions than D15. This shape change neither demonstrates crystallographic grain refinement nor

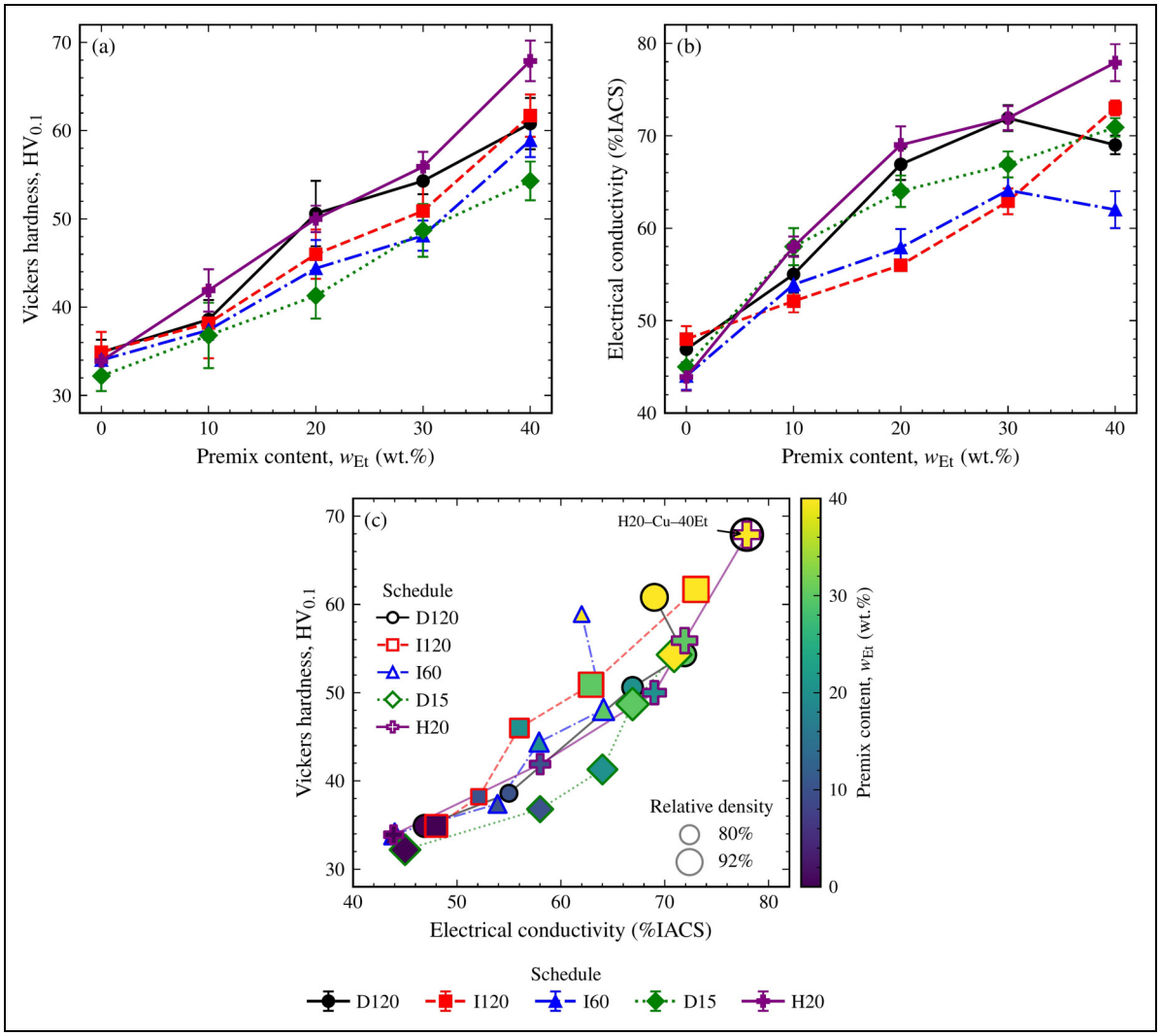


Figure 7. Effect of premix content and thermal schedule on properties: (a) Vickers hardness, (b) measured electrical conductivity and (c) hardness–conductivity map. Error bars in (a,b) denote one standard deviation for three independently processed compacts. In (c), colour represents premix content, shape identifies schedule and size increases with relative density. Rankings refer to observed means and do not imply statistically significant differences.

identifies a unique transport mechanism. H20 combined high density with finer Ag-rich intergranular features.

Figure 4(a) provides a descriptive comparison of the plotted Cu-rich size values. For Cu–20Et, the D120 value is smaller than those for I60 and I120; D120 has the largest value only for Cu–30Et and Cu–40Et. Thus, the plotted descriptor does not increase with prolonged high-temperature holding across all compositions. I120–Cu–40Et has a smaller plotted Cu-rich size value than D120–Cu–40Et. These comparisons describe the plotted ordering only: the unresolved measurement definitions in the 'Quantitative stereology' section preclude interpreting the values as verified median intercepts or using them to establish grain-growth kinetics. Pore refinement is assessed qualitatively from the micrographs, not from an assumed Feret or equivalent-circle interpretation of panel (b).

At the same D120 hold time, Figure 10(j) (Cu–40Et) contains locally smaller-looking Cu-rich regions than those in panel (i) (Cu–30Et). However, the plotted Cu-rich size descriptor in Figure 4(a) increases from Cu–30Et to Cu–40Et under D120, subject to the unresolved definition noted above. The selected fields therefore do not establish a composition-wide refinement trend. This comparison between compositions is distinct from the comparisons between schedules at fixed composition above.

Contiguity and dihedral angle decreased with premix content as Ag-rich material increasingly separated the Cu-rich regions.

Phase constitution and Cu/Ag redistribution

The XRD patterns contained Cu-rich and Ag-rich FCC reflections consistent with the equilibrium Cu–Ag system (Figure 11).[7] As measurements followed furnace cooling, they identify final crystalline phases but cannot confirm liquid formation or its onset temperature. SEM–EDS was used to assess schedule-dependent redistribution.

The main Cu-rich reflection shifted to lower 2θ in all premix-containing materials, indicating greater interplanar spacing by Bragg's law.[51] Along with EDS, this is consistent with retained Ag in Cu-rich solid solution, although residual strain, specimen displacement and calibration can also shift peaks. Cu–10Et had the broadest peak, smallest estimated crystallite size and highest microstrain. At higher premix

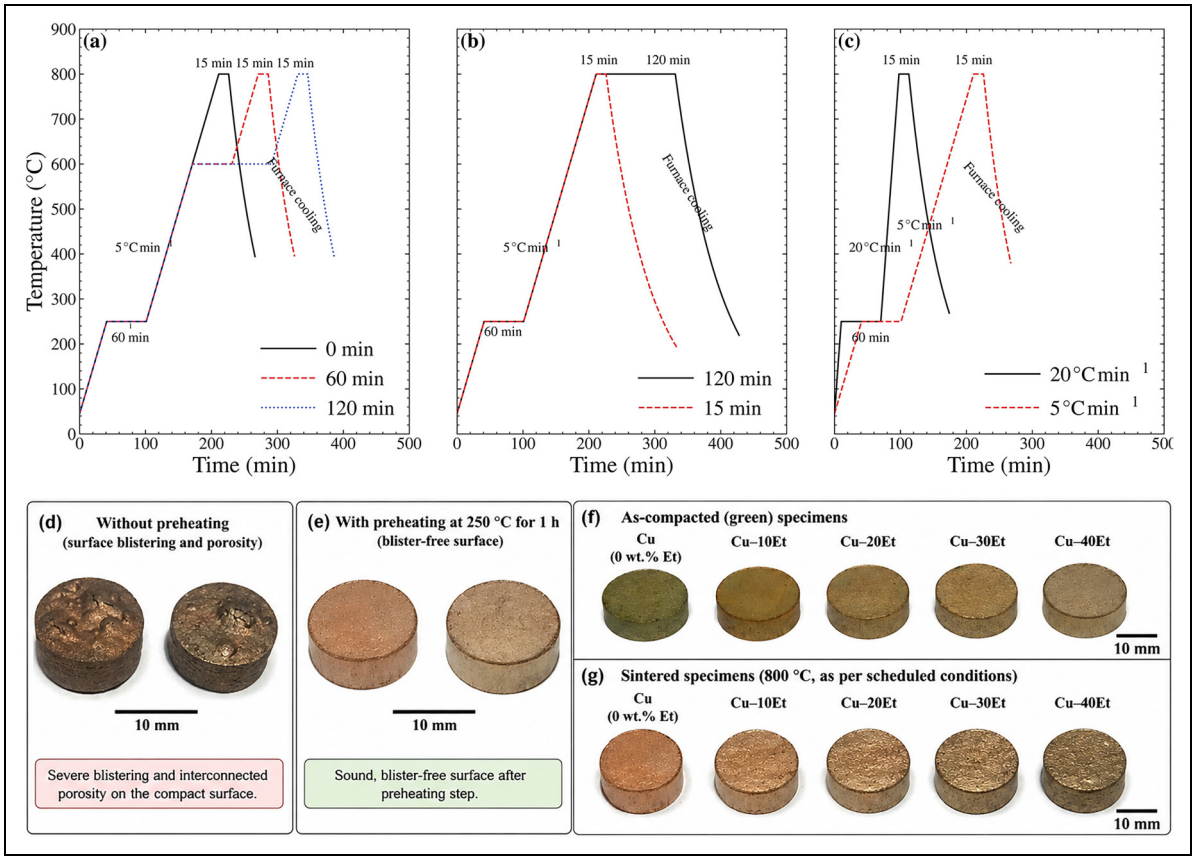


Figure 8. Cu–Et processing design: powder blending, compaction, thermal schedules, surface condition before and after preheating at 250 °C for 1 hour, and representative green and sintered compacts.

contents, crystallite size increased and microstrain decreased, indicating partial recovery of coherent diffracting regions.[52,53]

EDS mapping confirmed that grey regions were Cu-rich and bright intergranular regions Ag-rich (Figure 12). The I120 maps showed a more uniform Ag-rich network and finer pores than the I60 maps at high premix content; the heatmaps summarise local spot analyses for all compositions and schedules.

D120 Cu-rich spots contained ~3.3–9.2 wt.% Ag. Ag-rich spots in D120–Cu–20Et, D120–Cu–30Et and D120–Cu–40Et contained 94.2, 95.5 and 91.3 wt.% Ag, respectively, and thus measurable Cu. These local post-cooling values are not liquid compositions: on cooling, Ag-rich liquid can partition into Cu-rich and Ag-rich FCC solids as Cu solubility decreases.[7,59] The spots also do not represent the complete intergranular region, and narrow regions may include adjacent material within the EDS interaction volume.[60,61]

In both line scans (Figure 13), the Cu signal decreased as the Ag signal increased on entering the bright intergranular region; these trends reversed on leaving it. The overlapping interface signals indicate a finite compositional transition but not a diffusion distance, because the SEM–EDS interaction volume broadens the profiles.[60,61]

Hardness and conductivity

Hardness generally increased with premix content, with Cu–30Et and Cu–40Et giving the largest observed means (Figure 7). Ag addition, changes in intergranular microstructure and reduced porosity may contribute to this response. In sintered materials, pores reduce the effective load-bearing cross-section and can lower apparent indentation hardness, although their influence depends on the volume sampled by the indent.[62] The present measurements do not isolate these contributions. Cu–10Et hardened less, consistent with its limited densification and limited development of Ag-rich regions.

Conductivity also generally increased with premix content, although the schedule affected the trend. Reduced porosity and improved interparticle continuity can favour electrical transport in sintered materials,[62] whereas solutes, defects and interfaces contribute to electron scattering.[4,13] Zhang and Meng[63] also demonstrated that electrical resistivity varies with deformation-induced microstructural evolution in drawn Cu–Ag composites; this provides context for microstructural effects, not direct evidence for pressureless-sintering densification. Improved metallic continuity is a plausible explanation for the present conductivity trend, but its contribution relative to scattering was not quantified and the density-based interpretation remains subject to the consistency check in the ‘Densification and dimensional response’ section. For a given composition, finer-pored specimens were more conductive. Figure 7(c) combines these relationships in a hardness–conductivity map for all schedules: symbol colour represents premix content, symbol shape identifies the schedule and symbol size increases with relative density. The map therefore relates hardness and conductivity to both composition and relative density while retaining the processing condition of each specimen.

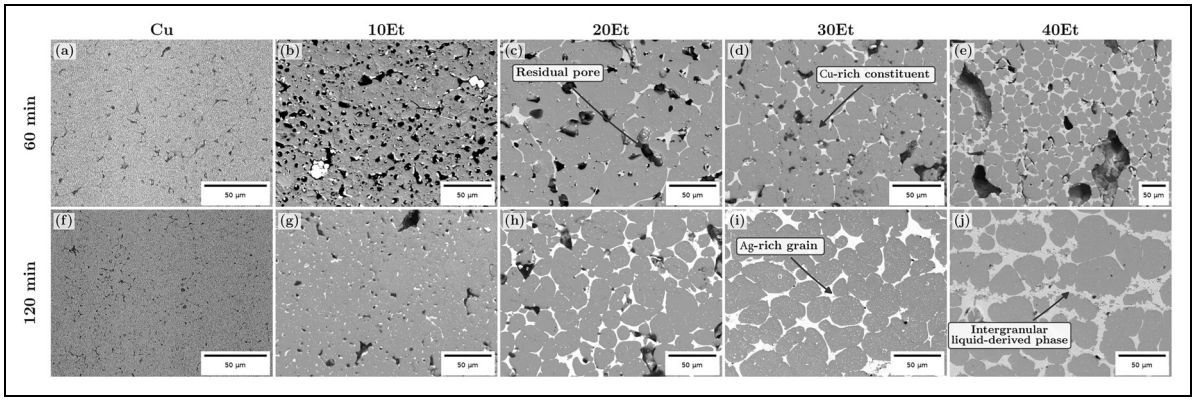


Figure 9. Backscattered electron (BSE) micrographs of Cu to Cu–40Et processed using (a)–(e) I60 and (f)–(j) I120. Bright regions are Ag-rich, grey regions are Cu-rich and dark regions are pores. Schedule codes are defined in Table 2.

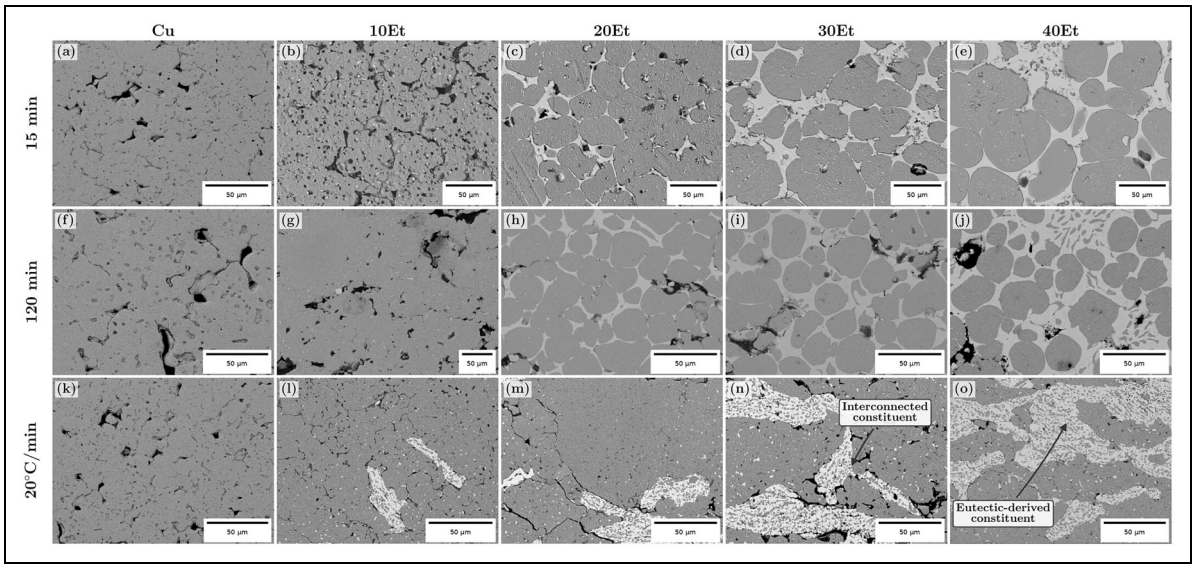


Figure 10. Backscattered electron (BSE) micrographs of Cu to Cu–40Et processed using (a)–(e) D15, (f)–(j) D120 and (k)–(o) H20. D120 produced more rounded Cu-rich regions, whereas H20 retained finer, less uniform Ag-rich intergranular features. Bright, grey and dark regions are Ag-rich material, Cu-rich material and pores, respectively.

H20–Cu–40Et gave the largest observed mean hardness and conductivity: (67.9 ± 2.3) $HV_{0.1}$ and (77.9 ± 2.0)% IACS, where the uncertainties are one standard deviation ($n = 3$ compacts). D120–Cu–40Et gave the largest observed mean density. These rankings are descriptive and do not establish statistical separation. Because H20 was not analysed stereologically, its properties cannot be related to the plotted Cu-rich size descriptor.

Discussion

Proposed liquid-phase-sintering sequence

Premix content and thermal history jointly controlled consolidation. Comparable effects of matrix fraction and presintering on porosity, stereology and mechanical response have been reported for liquid-phase-sintered W–Ni–Fe alloys.[64] Here, the density, microscopy and phase-analysis results are interpreted using the liquid-phase-sintering framework of German et al.[27,31,32] The following stages are a proposed sequence of overlapping processes, not a time-resolved experimental reconstruction.

(i) Heating and local liquid formation. Below the eutectic temperature, solid-state necking and Cu/Ag interdiffusion can alter the initial contact network and local compositions.[27] The I60 and I120 holds at 600 °C therefore provide additional time for these processes, not equilibrium liquid-phase sintering. On crossing ~779.1 °C, liquid is expected first in suitably composed Cu/Ag contact regions; the mechanically milled premix need not melt uniformly or completely.[7] The nominal 800 °C hold permits liquid formation, but neither its onset nor its spatial distribution was measured.

(ii) Transient versus persistent liquid. Using the reported ~800 °C tie-line compositions, Cu–10Et (7.20 wt.% Ag) lies close to, but below, the Cu-rich solidus. Any local contact liquid could be consumed as Ag redistributes into the Cu-rich solid: a possible transient-liquid contribution, not evidence that liquid necessarily formed

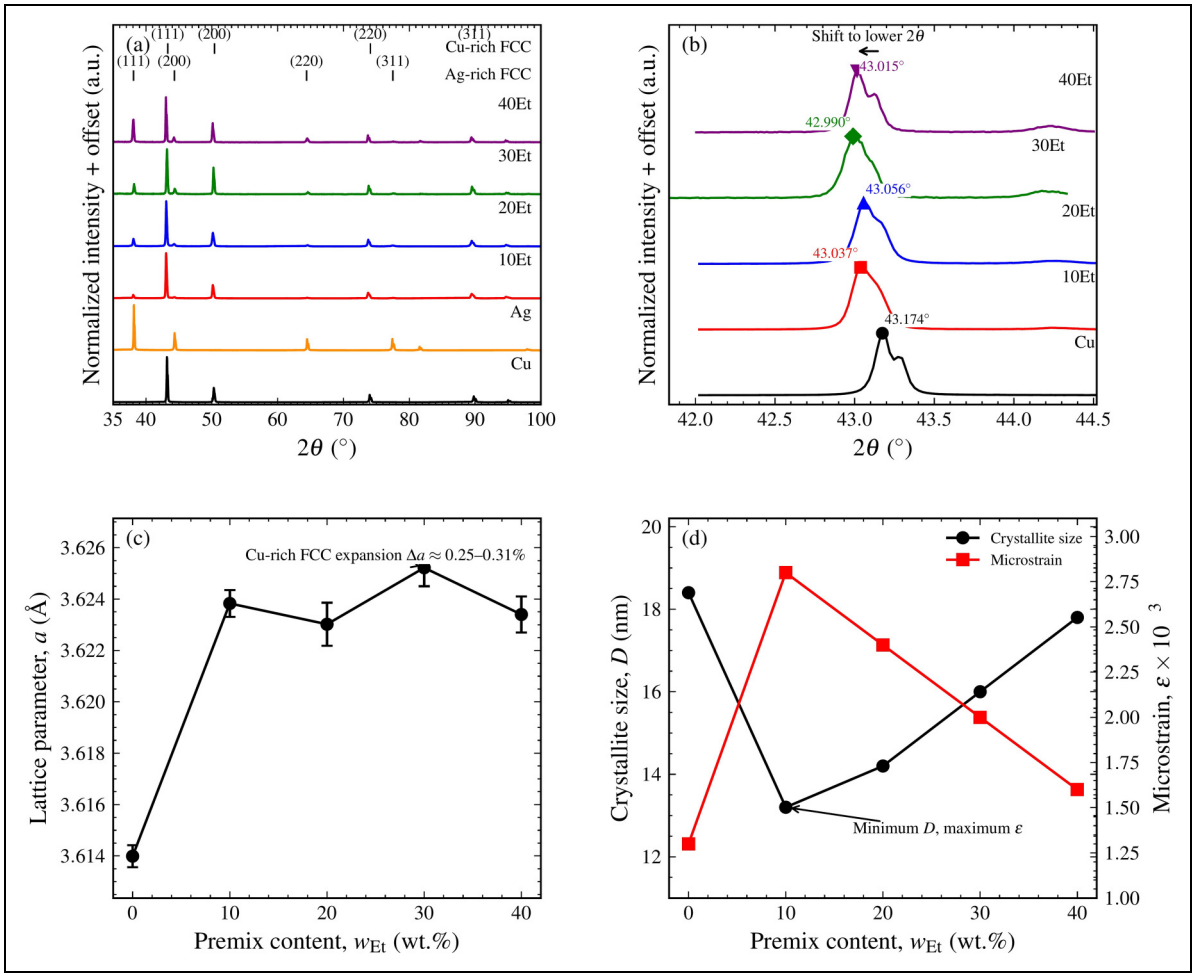


Figure 11. X-ray diffraction (XRD) analysis of the sintered Cu–Et series: (a) full patterns, (b) principal Cu-rich reflection, (c) Cu-rich lattice parameter, and (d) crystallite size and microstrain from pseudo-Voigt variance analysis.

or disappeared within the available hold. Cu–20Et, Cu–30Et and Cu–40Et instead lie in the Cu-rich solid + liquid field, with estimated equilibrium liquid mass fractions of 12%, 24% and 36%, respectively.[7] Persistent liquid is therefore expected for these compositions on approaching equilibrium. Ag dissolution into Cu can occur in either regime; it does not by itself demonstrate complete liquid consumption.[27] The weak densification response of Cu–10Et and greater response at higher additions (Figure 5) are consistent with this composition-dependent distinction, but do not measure liquid lifetime.

(iii) Spreading, rearrangement and pore accommodation. If the liquid wets Cu, capillary forces can redistribute it along accessible contacts and draw particles together.[27,31] Increasingly extensive Ag-rich boundary and junction regions in Figures 9 and 10, together with increased shrinkage, are consistent with liquid-assisted consolidation overcoming the poorer initial packing at high premix contents. Lower post-cooling contiguity and dihedral angles (Figure 4) describe greater separation of Cu-rich regions, but are not direct measurements of high-temperature wetting. The finer Cu–40Et pores and more uniform intergranular material after I120 than I60 suggest that the sub-eutectic history also influenced subsequent liquid distribution. Pore filling depends on pore geometry, liquid availability and wetting[65–67]; endpoint pore sizes alone cannot identify the controlling process.

(iv) Solution–reprecipitation and shape evolution during holding. Dissolution of Cu from high-curvature surfaces or stressed contacts, transport through the liquid and reprecipitation at lower-chemical-potential sites can accommodate shape changes and densification.[27,29,30] The more rounded Cu-rich regions after D120 than D15 (Figure 10) are compatible with such transport during prolonged liquid exposure. Rearrangement, coalescence and solid-state transport may also contribute; rounding alone neither proves solution–reprecipitation nor establishes persistent liquid. D120 gave the largest plotted Cu-rich size value only for Cu–30Et and Cu–40Et (Figure 4), so no universal size-growth trend is inferred. H20 retained finer, less uniform Ag-rich features despite high density, consistent with less time for redistribution during heating; a larger actual liquid fraction in H20 was not measured.

Possible local fragmentation. The smaller-looking regions in Figure 10(j) also motivate consideration of liquid-assisted breakup. The starting Cu powder in Figure 1(a) shows surface cavities and attached satellites, although this surface image does not establish internal pore connectivity. If wetting liquid enters accessible pores or weak interparticle contacts, dissolution of thin Cu walls

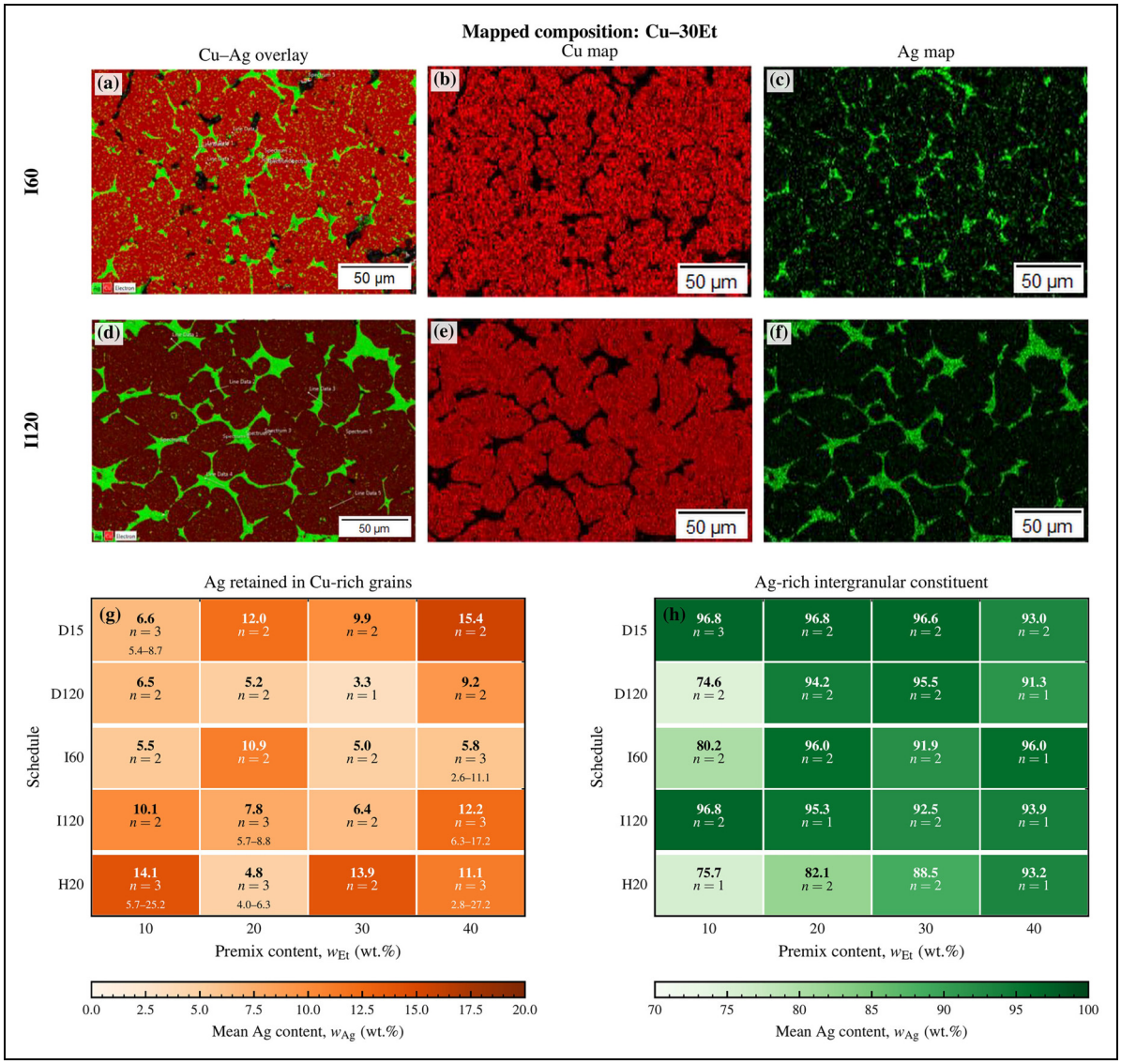


Figure 12. Cu/Ag redistribution after furnace cooling: BSE images and elemental maps for I60– and I120–Cu–30Et, with heatmaps of local Ag contents in final Cu-rich and Ag-rich solids for all schedules. Values are local post-cooling results, not liquid compositions or area averages; intermediate spots may include adjacent material within the EDS interaction volume. BSE: backscattered electron; EDS: energy-dispersive X-ray spectroscopy.

or satellite necks could separate parts of a porous particle or agglomerate. This hypothesis follows the general penetration–fragmentation mechanism described by German[31]; greater liquid availability at higher Et content could facilitate it where suitable pathways exist. It is not direct evidence of fragmentation in these specimens. The increase in the plotted D120 Cu-rich size descriptor from Cu–30Et to Cu–40Et does not support net refinement, while the two-dimensional region metric cannot track individual parent particles or exclude local breakup alongside coalescence and coarsening. Sectioning and field selection can also affect the visual comparison. Confirmation would require interrupted-hold observations of penetrating liquid and separating contacts, supported by three-dimensional imaging or particle-resolved size analysis.

(v) Solid-framework development and cooling. Retained and growing solid contacts can progressively restrict rearrangement while liquid remains between Cu-rich regions.[31,32] Shape retention is compatible with a mechanically stable solid framework, but does not establish its three-dimensional connectivity or a separately resolved final skeleton-sintering stage. Remaining liquid is expected to solidify during furnace cooling, with further Cu/Ag partitioning as solid solubilities decrease.[7,59] The final Cu-rich and Ag-rich FCC phases and intergranular EDS distributions (Figures 11 to 13) are compatible with this account, not direct records of the melt. Local post-cooling compositions cannot recover liquid composition, fraction or lifetime. DSC/DTA and in-situ or interrupted-hold observations would be needed to test the proposed sequence and distinguish its overlapping mechanisms.

Selection criterion and practical recommendation

Increasing premix content added electron-scattering solute and interfaces but also increased density and metallic continuity. The density gain dominated, so hardness and conductivity often rose together. For the stated objective of

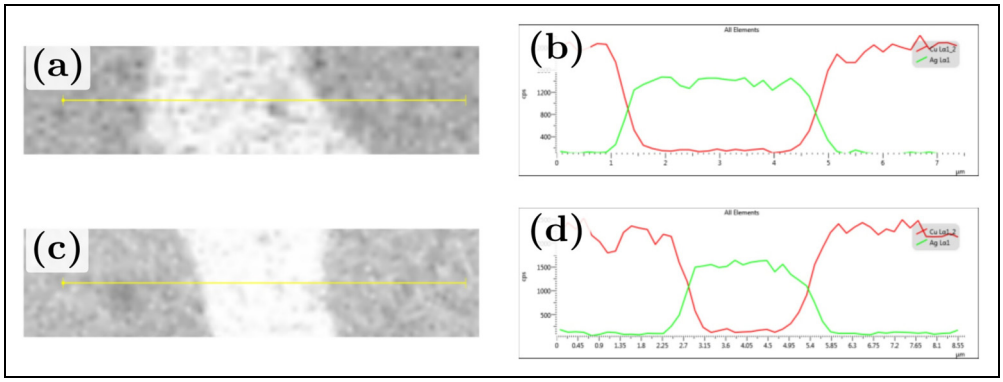


Figure 13. EDS line scans across two Cu-rich/Ag-rich interfaces: (a) and (c) line locations and (b) and (d) Cu K and Ag L profiles. Reciprocal signal changes identify the Ag-rich material; transition widths include broadening from the SEM–EDS interaction volume. EDS: energy-dispersive X-ray spectroscopy; SEM–EDS: scanning electron microscopy with energy-dispersive X-ray spectroscopy.

combining high conductivity with high hardness, these two properties are the primary selection criteria; density and high-temperature hold duration are evaluated as trade-offs. This is a qualitative engineering judgement based on the measured results, not a weighted optimisation or a claim that all properties can be maximised simultaneously.

H20–Cu–40Et is the single recommended condition within the tested set. It gave the largest observed mean hardness, (67.9 ± 2.3) $HV_{0.1}$, and conductivity, (77.9 ± 2.0)% IACS, together with ~92.2% relative density after 15 minutes at 800 °C (Figure 7). D120–Cu–40Et reached ~93.4% relative density after 120 minutes at that temperature. Thus, selecting H20 entails accepting a relative density about 1.2 percentage points lower in exchange for the highest observed means of both primary properties and a 105 minutes shorter high-temperature hold. This comparison concerns hold duration, not measured total cycle time, energy use or production cost. D120 is retained as the density benchmark, not as a second overall recommendation.

The recommendation applies to the tested compositions and schedules under the stated property priority. The observed rankings were not subjected to significance testing, and no application-specific acceptance limits or service tests were established. H20–Cu–40Et is therefore a candidate for further application-specific evaluation, not a statistically established or universally optimal material. A requirement prioritising maximum density would represent a different selection objective.

Conclusions

The main conclusions for the tested 0–40 wt.% Et range are:

1. Irregular, flattened premix agglomerates reduced green density at high additions, but the greater sintering response outweighed this packing penalty.
2. At 800 °C, Cu–10Et lies below the Cu-rich solidus, whereas Cu–20Et, Cu–30Et and Cu–40Et have estimated equilibrium liquid fractions of 12, 24 and 36 wt.%. Melting and liquid fraction were not measured in situ.
3. D120–Cu–40Et gave the largest observed mean relative density (~93.4%); H20–Cu–40Et reached ~92.2% after 15 minutes. I120–Cu–40Et had finer observed pores than I60–Cu–40Et.
4. Longer holding reduced pore size and rounded the Cu-rich regions, but increased the plotted Cu-rich size descriptor only for Cu–30Et and Cu–40Et. Rapid heating retained finer, less uniform Ag-rich features. Contiguity and dihedral angle decreased with Et content.
5. XRD and EDS showed Cu-rich and Ag-rich FCC phases with mutual elemental redistribution.
6. When combined hardness and conductivity are prioritised, with density and hold duration as trade-offs, H20–Cu–40Et is the single recommended tested condition: 67.9 ± 2.3 $HV_{0.1}$, 77.9 ± 2.0% IACS and ~92.2% relative density after 15 minutes at 800 °C. Relative to the D120–Cu–40Et density benchmark, this condition has a relative density about 1.2 percentage points lower and a high-temperature hold 105 minutes shorter. The recommendation is descriptive, without significance testing or application-specific validation; it is not a universal optimum.

Acknowledgements

The authors thank the Powder Metallurgy Laboratory, Indian Institute of Technology Kanpur, for fabrication support, and the Department of Materials Science and Engineering and Advanced Centre for Materials Science for access to SEM and mechanical-testing facilities.

ORCID iD

Mirtunjay Kumar https://orcid.org/0000-0002-5706-2283

Author contributions

Avinash Singh: conceptualisation, methodology, software, investigation, formal analysis, visualisation, and writing–original draft. Harish Ranot: validation, and writing–review and editing. Mirtunjay Kumar: formal analysis, methodology, visualisation, writing–original draft, and writing–review and editing. Anish Upadhyaya: supervision, funding acquisition, and writing–review and editing.

Funding

The authors received no financial support for the research, authorship, and/or publication of this article.

Declaration of conflicting interests

The authors declared no potential conflicts of interest with respect to the research, authorship, and/or publication of this article.

Data availability statement

The data that support the findings of this study are available from the corresponding authors upon reasonable request.

References

1. Davis JR. *Copper and Copper Alloys*. ASM International, 2001.
2. Matula RA. Electrical resistivity of copper, gold, palladium, and silver. *J Phys Chem Reference Data* 1979; 8: 1147–1298.
3. Mao Q, Liu Y and Zhao Y. A review on copper alloys with high strength and high electrical conductivity. *J Alloys Compd* 2024; 990: 174456.
4. Rossiter PL. *The Electrical Resistivity of Metals and Alloys*. Cambridge University Press, 1987.
5. Yang K, Wang Y, Guo M, et al. Recent development of advanced precipitation-strengthened Cu alloys with high strength and conductivity: a review. *Prog Mater Sci* 2023; 138: 101141.
6. Zhang WJ, Huang L, Mi XJ, et al. Researches for higher electrical conductivity copper-based materials. *cMat* 2024; 1: e13.
7. Subramanian PR and Perepezko JH. The Ag–Cu (silver-copper) system. *J Phase Equilibria* 1993; 14: 62–75.
8. Sakai Y, Inoue K, Asano T, et al. Development of high-strength, high-conductivity Cu–Ag alloys for high-field pulsed magnet use. *Appl Phys Lett* 1991; 59: 2965–2967.
9. Han K, Vasquez AA, Xin Y, et al. Microstructure and tensile properties of nanostructured Cu–25 wt.% Ag. *Acta Mater* 2003; 51: 767–780.
10. Zhang BB, Tao NR and Lu K. A high strength and high electrical conductivity bulk Cu–Ag alloy strengthened with nanotwins. *Scr Mater* 2017; 129: 39–43.
11. Sakai Y and Schneider-Muntau HJ. Ultra-high strength, high conductivity Cu–Ag alloy wires. *Acta Mater* 1997; 45: 1017–1023.
12. Benghalem A and Morris DG. Microstructure and strength of wire-drawn Cu–Ag filamentary composites. *Acta Mater* 1997; 45: 397–406.
13. Hong SI and Hill MA. Mechanical stability and electrical conductivity of Cu–Ag filamentary microcomposites. *Mater Sci Eng: A* 1999; 264: 151–158.
14. Lin J and Meng L. Effect of aging treatment on microstructure and mechanical properties of Cu–Ag alloys. *J Alloys Compd* 2008; 454: 150–155.
15. Watanabe C, Monzen R, Nagayoshi H, et al. Elastic state of rod-shaped Ag precipitates in a Cu–5.7 wt.% Ag single crystal. *Philos Mag Lett* 2006; 86: 65–73.
16. Gaganov A, Freudenberger J, Botcharova E, et al. Effect of Zr additions on the microstructure, and the mechanical and electrical properties of Cu–7 wt.% Ag alloys. *Mater Sci Eng: A* 2006; 437: 313–322.
17. Bao G, Xu Y, Huang L, et al. Strengthening effect of Ag precipitates in Cu–Ag alloys: A quantitative approach. *Mater Res Lett* 2016; 4: 37–42.
18. Zhao C, Zuo X, Wang E, et al. Simultaneously increasing strength and electrical conductivity in nanostructured Cu–Ag composite. *Mater Sci Eng: A* 2016; 652: 296–304.
19. Tian Y and Zhang Z. Microstructures and tensile deformation behavior of Cu–16 wt.% Ag binary alloy. *Mater Sci Eng: A* 2009; 508: 209–213.
20. Liu JB, Meng L and Zeng YW. Microstructure evolution and properties of Cu–Ag microcomposites with different Ag content. *Mater Sci Eng: A* 2006; 435–436: 237–244.
21. Choi EA, Lee SJ, Ahn J, et al. Enhancement of strength and electrical conductivity for hypo-eutectic Cu–12Ag alloy. *J Alloys Compd* 2023; 931: 167506.
22. Tardieu S, Mesguich D, Lonjon A, et al. High strength-high conductivity silver nanowire-copper composite wires by spark plasma sintering and wire-drawing for non-destructive pulsed fields. *IEEE Trans Appl Supercond* 2020; 30: 6900304.
23. Varol T, Güler O, Akçay SB, et al. Enhancement of electrical and thermal conductivity of low-cost novel Cu–Ag alloys prepared by hot-pressing and electroless plating from recycled electrolytic copper powders. *Mater Chem Phys* 2022; 281: 125892.
24. Robinson J, Munagala SP, Arjunan A, et al. Electrical conductivity of additively manufactured copper and silver for electrical winding applications. *Materials* 2022; 15: 7563.
25. Li J, Li Y, Wang Z, et al. Ultrahigh oxidation resistance and high electrical conductivity in copper-silver powder. *Sci Rep* 2016; 6: 39650.
26. German RM. *Sintering Theory and Practice*. John Wiley & Sons, 1996.
27. German RM, Suri P and Park SJ. Review: liquid phase sintering. *J Mater Sci* 2009; 44: 1–39.
28. Guillon O, Gonzalez-Julian J, Dargatz B, et al. Field-assisted sintering technology/spark plasma sintering: mechanisms, materials, and technology developments. *Adv Eng Mater* 2014; 16: 830–849.
29. Kingery WD. Densification during sintering in the presence of a liquid phase. i. Theory. *J Appl Phys* 1959; 30: 301–306.
30. Mortensen A. Kinetics of densification by solution-reprecipitation. *Acta Mater* 1997; 45: 749–758.
31. German RM. *Liquid Phase Sintering*. Plenum Press, 1985.
32. German RM. *Sintering: From Empirical Observations to Scientific Principles*. Butterworth-Heinemann, 2014.
33. Suryanarayana C. Mechanical alloying and milling. *Prog Mater Sci* 2001; 46: 1–184.
34. Suryanarayana C. Mechanical alloying: a novel technique to synthesize advanced materials. *Research* 2019; 2019: 4219812.
35. Pragatheeswaran A, Ravi R and Bakshi SR. Microstructural and morphological changes during ball milling of copper-silver-graphite flake mixtures. *Adv Powder Technol* 2019; 30: 2759–2767.
36. Ohsaki S, Kato S, Tsuji N, et al. Bulk mechanical alloying of Cu–Ag and Cu/Zr two-phase microstructures by accumulative roll-bonding process. *Acta Mater* 2007; 55: 2885–2895.
37. Tolmachev T, Pilyugin V, Ancharov A, et al. On the structural features of mechanically alloyed Cu–Ag and Au–Co by severe

cold and cryogenic plastic deformation. *Phys Procedia* 2016; 84: 349–354.
38. ASTM B212-17: Standard test method for apparent density of free-flowing metal powders using the Hall flowmeter funnel, 2017. DOI: 10.1520/B0212-17.
39. ASTM B527-20: Standard test method for tap density of metal powders and compounds, 2020. DOI: 10.1520/B0527-20.
40. ASTM B213-20: Standard test methods for flow rate of metal powders using the Hall flowmeter funnel, 2020. DOI: 10.1520/B0213-20.
41. Schneider CA, Rasband WS and Eliceiri KW. NIH image to ImageJ: 25 years of image analysis. *Nat Methods* 2012; 9: 671–675.
42. Ramakrishnan P. Sintering kinetics of oxide-film-coated copper powder. *Powder Metall* 1966; 9: 47–53.
43. Hübner CG, Staab T and Leipner HS. TEM studies of the microstructure of pressureless sintered copper. *Phys Stat Solidi (a)* 1995; 150: 653–660.
44. ASTM B962-17: Standard test methods for density of compacted or sintered powder metallurgy (PM) products using Archimedes' principle, 2017. DOI: 10.1520/B0962-17.
45. ASTM E3-11(2017): Standard guide for preparation of metallographic specimens, 2017. DOI: 10.1520/E0003-11R17.
46. DeHoff RT and Rhines FN. *Quantitative Microscopy*. McGraw-Hill, 1968.
47. Underwood EE. *Quantitative Stereology*. Addison-Wesley, 1970.
48. ASTM E1245-03(2016): Standard practice for determining the inclusion or second-phase constituent content of metals by automatic image analysis, 2016. DOI: 10.1520/E1245-03R16.
49. Warren R and Waldron MB. Microstructural development during the liquid-phase sintering of cemented carbides: I. Wettability and grain contact. *Powder Metall* 1972; 15: 166–201.
50. Kumar M, Ranot H, Kamal T, et al. Automated quantification of dihedral angles in sintered tungsten heavy alloys using image processing. *Int J Refract Metals Hard Mater* 2026; 134: 107467.
51. Bragg WH and Bragg WL. The reflection of X-rays by crystals. *Proc R Soc A* 1913; 88: 428–438.
52. Klug HP and Alexander LE. *X-ray Diffraction Procedures for Polycrystalline and Amorphous Materials*. 2 ed. John Wiley & Sons, 1974.
53. Langford JI. A rapid method for analysing the breadths of diffraction and spectral lines using the Voigt function. *J Appl Crystallogr* 1978; 11: 10–14.
54. ASTM E1508-12a(2019): Standard guide for quantitative analysis by energy-dispersive spectroscopy, 2019. DOI: 10.1520/E1508-12AR19.
55. ASTM E384-22: Standard test method for microindentation hardness of materials, 2022. DOI: 10.1520/E0384-22.
56. ASTM E1004-17: Standard test method for determining electrical conductivity using the electromagnetic (eddy current) method, 2017. DOI: 10.1520/E1004-17.
57. Reed JS. *Principles of Ceramics Processing*. 2 ed. John Wiley & Sons, 1995.
58. Shui A, Uchida N and Uematsu K. Origin of shrinkage anisotropy during sintering for uniaxially pressed alumina compacts. *Powder Technol* 2002; 127: 9–18.
59. Qin Q, Li J, Yang L, et al. Solidification behavior and microstructure of Ag–Cu eutectic alloy at different sub-rapid cooling rates. *Mater Chem Phys* 2024; 311: 128521.
60. Goldstein JI, Newbury DE, Michael JR, et al. *Scanning Electron Microscopy and X-ray Microanalysis*. 4 ed. Springer, 2018.
61. Drouin D, Couture AR, Joly D, et al. CASINO V2.42—a fast and easy-to-use modeling tool for scanning electron microscopy and microanalysis users. *Scanning* 2007; 29: 92–101.
62. Ternero F, Rosa LG, Urban P, et al. Influence of the total porosity on the properties of sintered materials—a review. *Metals* 2021; 11: 730.
63. Zhang L and Meng L. Evolution of microstructure and electrical resistivity of Cu–12 wt.% Ag filamentary microcomposite with drawing deformation. *Scr Mater* 2005; 52: 1187–1191.
64. Kumar M, Kamal T, Ranot H, et al. Effect of matrix content and pre-sintering-assisted liquid-phase sintering on the microstructure, stereology, and mechanical behavior of W–Ni–Fe tungsten heavy alloys. *Int J Refract Metals Hard Mater* 2026; 140: 107922.
65. Lee SM and Kang SJL. Theoretical analysis of liquid-phase sintering: pore filling theory. *Acta Mater* 1998; 46: 3191–3202.
66. Lu K, Xu X, Yi W, et al. Porosity effect on densification and shape distortion in liquid phase sintering. *Mater Sci Eng: A* 2001; 318: 111–121.
67. Kim YP, Jung SW, Kang SJL, et al. Enhanced densification of liquid-phase-sintered WC–Co by use of coarse WC powder: experimental support for the pore-filling theory. *J Am Ceramic Soc* 2005; 88: 2106–2109.